ACS Energy LETTERS

http://pubs.acs.org/journal/aelccp

Reaction Mechanism of Photocatalytic Hydrogen Production at Water/Tin Halide Perovskite Interfaces

Damiano Ricciarelli, Waldemar Kaiser, Edoardo Mosconi, Julia Wiktor, Muhammad Waqar Ashraf, Lorenzo Malavasi, Francesco Ambrosio,* and Filippo De Angelis*

Cite This: *ACS Energy Lett.* 2022, 7, 1308−1315

Read Online

ACCESS | Metrics & More | Article Recommendations | Supporting Information

ABSTRACT: While instability in aqueous environment has long impeded employment of metal halide perovskites for heterogeneous photocatalysis, recent reports have shown that some particular tin halide perovskites (THPs) can be water-stable *and* active in photocatalytic hydrogen production. To unravel the mechanistic details underlying the photocatalytic activity of THPs, we compare the reactivity of the water-stable and active $DMASnBr_3$ (DMA = dimethylammonium) perovskite against prototypical $MASnI_3$ and $MASnBr_3$ compounds (MA = methylammonium), employing advanced electronic−structure calculations. We find that the binding energy of electron polarons at the surface of THPs, driven by the conduction band energetics, is cardinal for photocatalytic hydrogen reduction. In this framework, the interplay between the A-site cation and halogen is found to play a key role in defining the photoreactivity of the material by tuning the perovskite electronic energy levels. Our study, by elucidating the key steps of the reaction, may assist in development of more stable and efficient materials for photocatalytic hydrogen reduction.

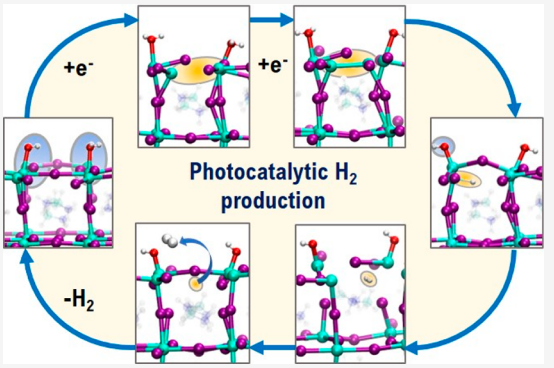

Metal halide perovskites are promising materials for photovoltaics due to their high absorption coefficients, long lifetimes of photogenerated carriers, and defect tolerance.[1−21] For these characteristics, lead-based materials, have, in particular, rapidly surged as competitors of silicon in the photovoltaics landscape.[22,23] A credible alternative to reduce the potential toxicity of lead-containing materials is the replacement of lead by tin.[24−27] Despite the lower band gap of tin halide perovskites (THPs), if compared to similar lead-based materials, the resulting solar cells remain limited in efficiency and stability due to the perovskite self-p-doping[28,29] and the facile Sn(II) → Sn(IV) oxidation associated with the formation of efficiency-limiting carrier traps.[28,30,31] THPs are in principle appealing also as photocatalysts because of their band edge tunability,[32] which permits a favorable alignment with redox potentials in aqueous environment.[29] Furthermore, THPs can efficiently localize electrons either through the formation of polarons in the pristine material or via defect-assisted processes involving halide vacancies or tin interstitials.[29,33] Since hydrogen reduction from heterogeneous water splitting implies the formation of either a $H^{\bullet}$ radical or of a H^- anion, i.e., the transfer of one or two electrons to a formal H^+ species, electron trapping at the surface may be key in assisting the overall reaction.[34−39]

Although potentially suitable for photocatalysis,[40] metal halide perovskites are usually unstable upon moisture and water exposure,[41−45] thus limiting the application of these materials in aqueous environment. This paradigm has been recently shifted with reports of novel perovskites which are *both* lead-free and water-stable.[46−51] Encouraging results have been obtained for Bi-based and Sn-based perovskites, which have shown not only water stability but also good photocatalytic properties.[46−51] In particular, dimethylammonium tin bromide ($DMASnBr_3$) is water-stable, as well as $DMASnI_3$;[52] it has a suitable band gap (∼2.8 eV)[47,53] and band edges well positioned with respect to the redox levels of liquid water.[46] While early reports measured hydrogen production rates of

Received: January 17, 2022
Accepted: March 7, 2022
Published: March 9, 2022

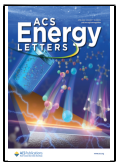

only a few μmol g^{-1} h^{-1},[47] the efficient charge carriers separation in perovskite/g-C_3N_4 composites was found to boost the activity with rates up to >1700 μmol g^{-1} h^{-1}.[46]

Motivated by the huge interest in THPs as effective photocatalysts for hydrogen production, we employ high-level density functional theory calculations to carry out a comparative analysis of the prototypical tin perovskites $MASnI_3$ (MA = methylammonium, Figure 1a–c) and

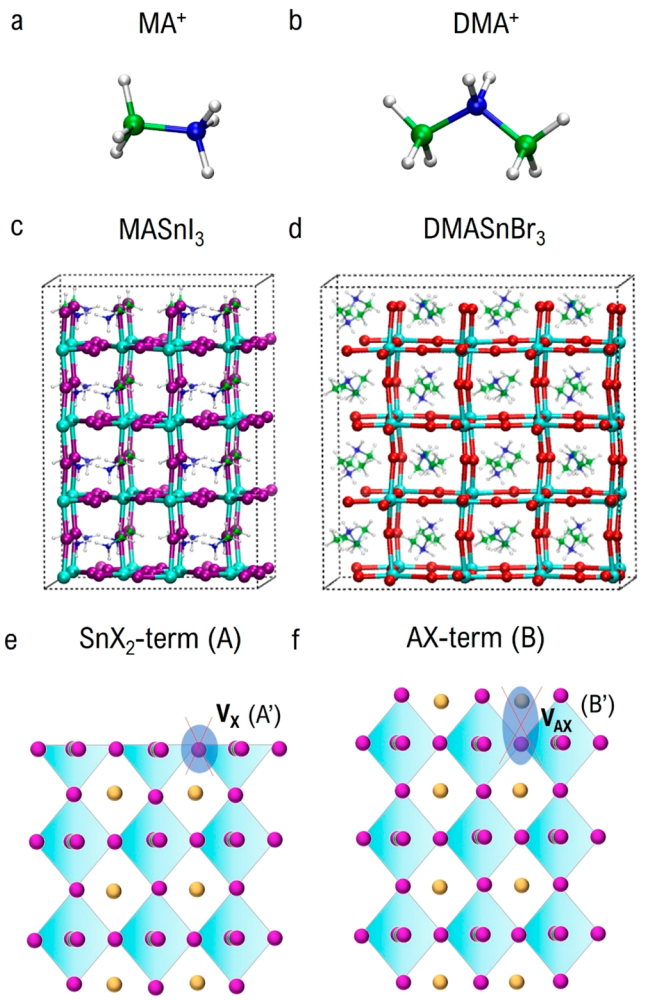

Figure 1. Chemical structures of (a) methylammonium and (b) dimethylammonium (green spheres for C, blue for N, and white for H). Bulk supercells of (c) $MASnI_3$ and (d) $DMASnBr_3$ (Sn atoms in cyan, I in violet, Br in red, C in green, N in blue, and H in white). Representation of the (001) perovskites slabs studied in this work: (e) model A for pristine and model A′ for halide vacant SnX_2-term slabs, and (f) model B for pristine and model B′ for Schottky containing AX-term slabs (purple (yellow) spheres for X halide (A cation)).

$MASnBr_3$ and the water-stable $DMASnBr_3$ (DMA = dimethylammonium, Figure 1b–d).[46] For the considered materials, we assess the electronic structure and, for $MASnI_3$ and $DMASnBr_3$, we calculate the binding energies of polarons and defects for different slabs. We also simulate the interaction between the perovskite and water, and we eventually reconstruct the overall hydrogen production reactivity pattern considering both SnX_2- and AX-terminated surfaces (Figure 1e,f, respectively). Our comparative analysis reveals that the binding energy of surface electron polarons, determined by conduction band energetics, has a dual role in the photocatalytic hydrogen production: while providing the main driving force for the reaction, trapping may hinder electron transfer toward hydrogen reduction. The chemical composition of the material, in terms of A-site cation and halogen, is found to play a key role in defining the photoreactivity of the material by tuning the perovskite electronic energy levels. Our study, by elucidating the key steps at the interfacial photocoupled electron transfer reaction, may assist the development of more stable and efficient materials for photocatalytic hydrogen reduction.

We first comment on the electronic structure of the bulk perovskites by employing the supercells reported in Figure 1c,d and using a hybrid HSE06-SOC[54,55] methodology benchmarked in previous studies (see the Supporting Information for further details).[26,29] The density of states (DOS; see the Supporting Information) shows a sizable tuning of the material band edges contributed by the interplay of the A-site cations and the halides: the calculated band gap increases from 1.1 eV in $MASnI_3$ to 3.2 eV in $DMASnBr_3$ as a result of a valence band (VB) (conduction band (CB)) down (up) shift of ∼0.8 eV (∼1.2 eV). The valence band energy stabilization for $DMASnBr_3$ should reduce the exposure of the material to oxidants, restoring a value similar to $MAPbI_3$,[29] healing the material from degradation into Sn^{4+} phases and self-p-doping effects.

The atomic contributions for the THPs are similar, with a a valence band more contributed by halogen atoms, and a conduction band mainly characterized by Sn atoms, while the organic framework does not contribute to the band edges. The composition of the CB suggests that, upon photoexcitation, electrons are more likely localized on Sn-sites. Therefore, polarons/defects connected to Sn chemistry may indeed be key for mediating charge transfer from the THP to protons.

Furthermore, to disentangle the halogen effect from that of the A-site cation on the electronic structure of $DMASnBr_3$, we consider a cubic $MASnBr_3$ perovskite from a previous study.[56] Our calculations highlight a low impact of the halogen on the CB, if compared to $MASnI_3$, with a slight upshift of 0.25 eV, while the VB shows a sizable downshift of 0.56 eV; see the Supporting Information. This possibly indicates that the A-site cation is, for the same halide, mostly tuning the CB upshift.

Next, we investigate the electronic structure of selected surfaces. To this end, given the similarity in the CB energetics achieved with HSE06-SOC and the semilocal PBE functional[54,57] (Supporting Information), we carry out our analysis using the latter for computational convenience, checking for hybrid-DFT/SOC effects in selected cases. We employ pre-existing models of the (001) surface implemented by some of us.[45] In particular, to account for the effects associated with different cation halide coverages and since the expected degree of AX coverage in water solutions is not trivial, we consider both a SnX_2 termination, model A in Figure 1e, and AX termination, model B in Figure 1f. The conduction band of the former is dominated by bulk contributions, while the latter favors electron localization on the surfaces.[45] To include the possibility of defect-mediated charge-trapping processes, we construct two additional slabs including a halide vacancy, V_X in the SnX_2-terminated surface, hereafter model A′ (Figure 1e), and a surface cation/halide vacancy (Schottky defect),[58] V_{AX} in the AX-terminated surface, hereafter B′ (Figure 1f) (see Supporting Information for additional details). The choice of different defect states is justified by the practical motivation of

https://doi.org/10.1021/acsenergylett.2c00122
ACS Energy Lett. 2022, 7, 1308–1315

avoiding disorder of organic cations due to the fictitious positive charge.[59] For the aim of our study, V_X and V_{AX} are equivalent, as they share identical trap states provided by undercoordinated tin atoms.[29]

Trapping of electrons at a surface site is an essential step for initiating the hydrogen evolution reaction, since this phenomenon creates a negatively charged hotspot. This process can be mediated either by formation of polarons in the pristine material or by the presence of defects connected to Sn coordination, in our case V_X or V_{AX}. In tin halide perovskites, trapping occurs from two types of atomic distortions occurring simultaneously, the movement of two Sn atoms belonging to neighboring SnX_6 octahedra toward each other and the out-of-plane shift of one Br atom, as shown in Scheme 1a; the latter is indeed not present in case of halide

Scheme 1. (a) Schematic Representation of Small Electron Polaron Formation in Tin Halide Perovskites;[33] Meaning of Polarons Binding Energies, E_1, for (b) Non-successful Electronic Trapping and (c) Successful Electronic Trapping[a]

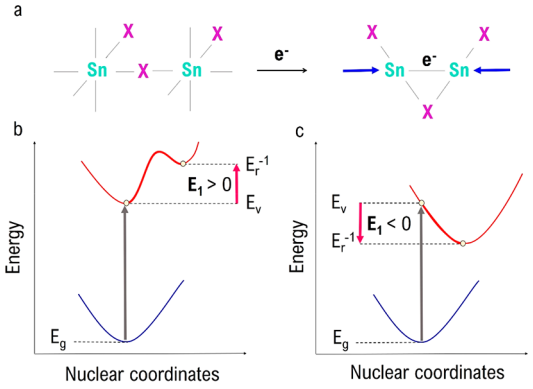

[a]In case b the polaron is a high-lying local minimum and the charge is preferentially delocalized in the conduction band, while in case c the vertical excitation is followed by an energy relaxation linked to charge localization. Other key quantities are, E_r^{-1}, the relaxation energy of the photocharged system, E_v, the energy associated to the vertical transition and E_g, the energy of the ground state.

vacancy defects.[33] The polaron binding energy, E_1 in Scheme 1, allows us to directly compare the trapping activity of different materials. A positive value of E_1, Scheme 1b, is connected with an endothermic polaron formation, with electron delocalization on the conduction band being favored, if compared to localized trapping. A negative E_1 value, Scheme 1c, indicates favorable electron localization. The same reasoning applies when considering the localization of two electrons and the respective bipolaron binding energy, E_2.

E_1 and E_2 are defined as the difference between $E_r^{-1/-2}$, polaron relaxation energy, and E_v, vertical transition energy, employing formulas 1 and 2,

$$E_1 = E_r^{-1} - E_g - \mathrm{CB} \quad (1)$$

$$E_2 = E_r^{-2} - E_g - 2\mathrm{CB} \quad (2)$$

where we approximate the vertical transition, E_v, by adding the energy of the conduction band, CB, to the ground state one E_g (twice in the case of E_2). The excited state of the system is here modeled by adding one or two extra electrons to the neutral system. Although this procedure neglects the hole left in the VB of the material, it represents a reasonable strategy to describe the behavior of the electrons after their vertical promotion to the conduction band; see the Supporting Information for details.

Binding energies reported in Figure 2 allow us to capture three key points: (i) a more arduous electron trapping in

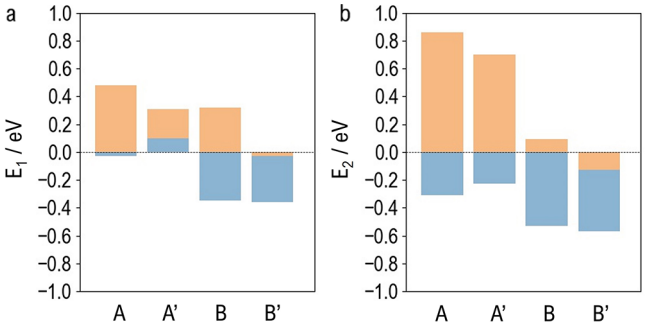

Figure 2. Monoelectronic and bielectronic trapping activity of $MASnI_3$ and $DMASnBr_3$. Calculated values of (a) E_1 and (b) E_2 for each considered surface model are represented by colored bars.

$MASnI_3$, which is significantly less favored compared to $DMASnBr_3$; (ii) the AX coverage modulates charge localization; and (iii) defects help in stabilizing localized electrons. In particular, the values calculated for $DMASnBr_3$ stem from a different position of the CB with respect to $MASnI_3$: in fact, a higher CB generally implies a larger energy gain when in-gap states are populated in the semiconductor. Internal differences between A and B models are connected with the different surface/bulk contributions to CB, with B delivering the maximum of surface contribution to the CB electron density and hence more probable charge localization of excitonic electrons.[45]

When considering injection of a single electron, we find that only the B/B′ models of $DMASnBr_3$ entails a significant binding energy (∼− 0.3 eV), while trapping is found to be generally unfavorable or marginally stabilized for the remaining systems. Local minima associated with electron trapping on the fully unpassivated surface of $MASnI_3$ entail localization on a lone Sn 5p state (cf. Figures 3a for the A model and S4 of the Supporting Information for A′). In contrast, for passivated surfaces, electron localization is accompanied by the formation of a Sn−Sn dimer (cf. Figure 3b). Upon addition of a second electron, charge localization is always found to be associated with formation of Sn−Sn dimers, showing bond lengths ranging from 3.1 to 3.3 Å (cf. Figure 3c,d). For $MASnI_3$, we calculate a negative value of E_2 only for the B′ model (∼− 0.2 eV), while electron localization is energetically favorable for all of the considered $DMASnBr_3$ surfaces (cf. Figure 2b). However, it should be noted that the unfavorable energetics for the trapping of the first electron implies that the formation of a bipolaron might be hindered for A/A′ models.

Next, we analyze perovskite/water interactions. First, we comment on the reported enhanced stability of $DMASnX_3$ in water[46,47,52] This can be related to the calculated solvation energies of dimethylammonium and methylammonium (cf. the Supporting Information). In particular, the reduced hydrophilicity of the dimethylammonium cation and the substitution of one H, no longer suitable for hydrogen bonds, with a methyl group make solvation less favorable.

https://doi.org/10.1021/acsenergylett.2c00122
ACS Energy Lett. 2022, 7, 1308−1315

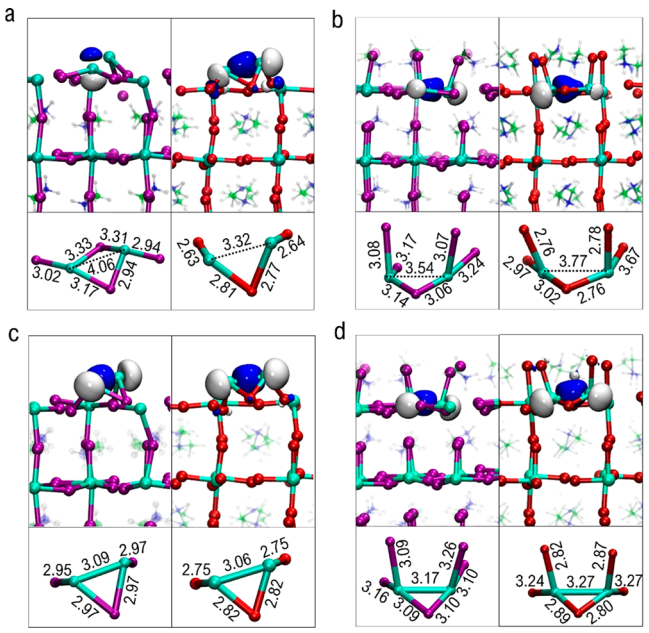

Figure 3. Isodensity representation of highest occupied molecular orbitals for polaronic (a, b) and bipolaronic (c, d) structures. Each system is accompanied by a detailed ball-and-stick representation of the local lattice distortions leading to charge localization. $SnIX_2$-terminated A models are depicted in panels a and c, while AX-terminated B models are portrayed in panels b and d. For each model, both $MASnI_3$ and $DMASnBr_3$ surfaces are shown.

We consider the binding of a H_2O molecule on a surface Sn-site, Figure 4a, and we define the adsorption energy, $\Delta E_{ads}(H_2O)$, from eqs 3 and 4:

$$H_2O(g) + \text{slab} \rightarrow H_2O(\text{ads}) \quad (3)$$

$$\Delta E_{ads}(H_2O) = E[H_2O(\text{ads})] - E[H_2O(g)] - E(\text{slab}) \quad (4)$$

where $E[H_2O(\text{ads})]$ is the total energy of the slab with an adsorbed water molecule and $E[H_2O(g)]$ and $E(\text{slab})$ are those of the isolated water molecule and of the slab, respectively. We note that for the fully covered AX-terminated surface (i.e., B model), subsurface Sn-sites are not available to interact with water. Therefore, in this case, we consider the replacement of a surface AX unit with a water molecule (cf. Figure 4b) and we define $\Delta E_{sub}(H_2O)$ the substitutional energy associated with this process:

$$H_2O(g) + \text{slab} \rightarrow H_2O(\text{sub}) + \text{AX} \quad (5)$$

$$\Delta E_{sub}(H_2O) = E[H_2O(\text{sub})] + E(\text{AX}) - E[H_2O(g)] - E(\text{slab}) \quad (6)$$

where $E[H_2O(\text{sub})]$ is the total energy of the slab with a water molecule replacing a AX unit and $E(\text{AX})$ the total energy of a AX pair.

Calculated values of $\Delta E_{ads}(H_2O)$ (cf. Figure 4d) indicate that the differences between the perovskites, surface terminations, and pristine/defective systems is exiguous, the energetics of adsorption deriving mainly from the Sn−O chemical bond. Differently, $\Delta E_{sub}(H_2O)$ values (cf. Figure 4e) denote that substitution is endothermic (exothermic) for $MASnI_3$ ($DMASnBr_3$). By decomposing $\Delta E_{sub}(H_2O)$ into the sum of the formation energy of a Schottky defect V_{AX} on the B surface and water adsorption energy on B′, we observe that

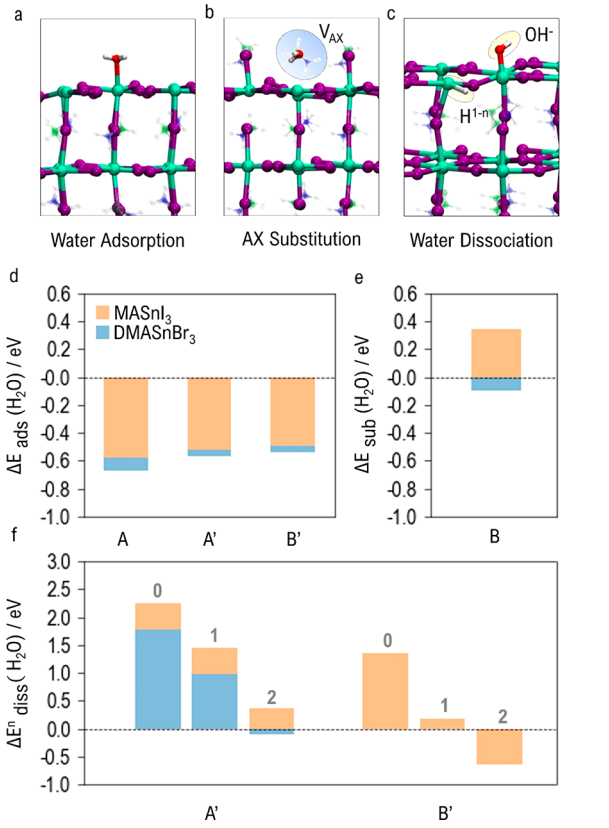

Figure 4. Representative structure of (a) of H_2O adsorbed on the THP surface. (b) H_2O substituting a surface AX unit of a B′ surface, and (c) H_2O dissociated on the THP surface. Exemplary structures are reported for $MASnI_3$. Calculated values of $\Delta E_{ads}(H_2O)$ (d), $\Delta E_{sub}(H_2O)$ (e), and $\Delta E_{dis}(H_2O)$ (f). Cf. main text for the definition of the quantities.

such a difference originates from the energy cost to create the Schottky defect, ∼0.8 eV in $MASnI_3$ vs ∼0.4 eV in $DMASnBr_3$. These results importantly forecast an increased probability to find H_2O molecules adsorbed on surface Sn atoms on $DMASnBr_3$ surface rather than on $MASnI_3$.

Then, we study the ability of the THPs to dissociate water molecules. This process is pivotal for generating molecular H_2, and it can occur either in the ground or in the excited state of the semiconductor. We simulate the dissociation energy for different charge states, $\Delta E_{diss}{}^n(H_2O)$ (neutral, $n = 0$, and under photocharging conditions, $n = 1, 2$), following eqs 7 and 8:

$$H_2O(\text{ads}) + ne^- \rightarrow OH(\text{ads})^- + H(\text{ads})^{1-n} \quad (7)$$

$$\Delta E_{dis}(H_2O) = E[OH(\text{ads})^- + H(\text{ads})^{1-n}] - E[H_2O(\text{ads}) + ne^-] \quad (8)$$

where $[OH(\text{ads})^- + H(\text{ads})^{1-n}]$ is the total energy of a system in which a $H_2O(\text{ads})$ is replaced by a $OH(\text{ads})^-$ with the dissociated H being adsorbed on a second Sn-site (cf. Figure 4c), while $E[H_2O(\text{ads}) + ne^-]$ is the total energy of the slab + molecular H_2O with n extra electrons.

Results collected for A′ and B′ models in Figure 4f indicate that, for both materials, the dissociation of water is significantly disfavored with $\Delta E^0_{diss}(H_2O) > 1.5$ eV for all considered models. At variance, products of reaction 7 are found to get progressively stabilized under electron rich conditions. In particular, when two electrons are captured, thus forming a surface hydride species, dissociation energies are drastically

https://doi.org/10.1021/acsenergylett.2c00122
ACS Energy Lett. 2022, 7, 1308−1315

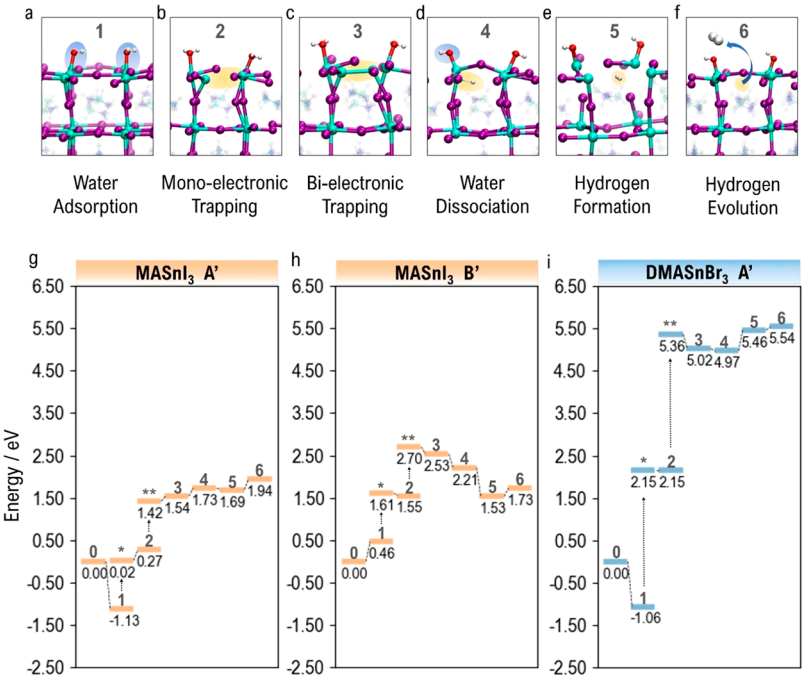

Figure 5. Hydrogen evolution reactivity for $MASnI_3$ and $DMASnBr_3$. Intermediates and products occurring in the simulated hydrogen evolution reaction: (a) adsorption of two H_2O molecules, (b) trapping of one electron at the Sn-site, (c) trapping of two electrons (d), dissociation of H_2O into OH^- + H^-, (e) hydrogen formation, (f) hydrogen evolution. The mechanism is illustrated for the A′ model of $MASnI_3$. (g−i) Reaction profiles for $MASnI_3$ (A′ and B′ models) and $DMASnI_3$ (A′ model). Energy values are referred to the ground state of the respective system. Vertical arrows followed by one and two asterisks indicate single and double excitations of the material, respectively.

decreased, with lowest values calculated (i) for $DMASnBr_3$, again in virtue of its higher CB, and (ii) for AX-covered surfaces, due to their larger surface contribution to the CB electron density. Overall, the present results suggest that the tendency toward electron-trapping-mediated water dissociation correlates with the electron-trapping properties, which in turn are modulated by the position of the CB. However, as previously observed, this is true also for electron localization on surface Sn−Sn dimers, thus hinting at a possible role of polarons in the hydrogen reduction reaction.

To fully understand the reactivity of THPs toward photocatalytic hydrogen reduction, we model the overall reaction:

$$2H_2O + 2e^- \rightarrow 2OH(ads)^- + H_2(g) \quad (9)$$

To this end, we construct possible pathways connecting reactants to products for A′ and B′ models of $MASnI_3$ and for the A′ model of $DMASnBr_3$, in order to account for both differences in the reactivity of the two different materials, and different AX coverages. Specifically, we study the reactants and the products of reaction 9, and the systems corresponding to the intermediate steps illustrated in Figure 5a−f.

Comparing the results for A′ models, we observe that electron trapping and water dissociation are more feasible for $DMASnBr_3$, a result in line with the previous discussion, but we also capture new interesting features: $DMASnBr_3$ presents a significant thermodynamic barrier (∼0.5 eV) for hydrogen generation connected with electron transfer from the Sn trap to adsorbed protons; cf. the energies of intermediates 4 and 5. Therefore, while a higher CB allows for a more efficient electron localization, this in turn can also hinder electron transfer toward the adsorbed proton. On the other hand, $MASnI_3$ has a more suitable band gap with less energy required for exciton generation. Moreover, the reaction steps toward H_2 formation are essentially barrierless. However, electron localization, which is central to the photocatalytic process, is energetically viable only when considering a high MAI coverage. In fact, for the fully unpassivated surface, charge localization is significantly disadvantaged (cf. Figure 5g). Overall, these results highlight that the interplay of the cation and halide is definitely an important parameter, since it modulates the stability and the photocatalytic efficiency of THPs.

In conclusion, we carried out an extensive analysis of the electron-trapping and photocatalytic activity of THPs, by considering the archetypal $MASnI_3$ and the recently synthesized water-stable and photoreactive $DMASnBr_3$. Our results show that the occurrence of electron polarons at the surface of THPs, whose binding energy is closely correlated with the position of the conduction band edge, plays an apical role in the photocatalytic hydrogen reduction reaction. In fact, it represents the main driving force for the reaction but, at the same time, a large stabilization of the trapped charge may be detrimental for the charge transfer toward the adsorbed proton, thus hindering the swift completion of the reaction. In this context, since the photoreactivity of THPs stems from the position of their electronic energy levels, the interplay between A-site cation and halogen in tuning such a property can be exploited toward the development of more stable and efficient materials for photocatalytic hydrogen reduction.

■ ASSOCIATED CONTENT

Supporting Information

The Supporting Information is available free of charge at https://pubs.acs.org/doi/10.1021/acsenergylett.2c00122.

https://doi.org/10.1021/acsenergylett.2c00122
ACS Energy Lett. 2022, 7, 1308−1315

Computational details; electronic structure of $MASnI_3$ vs $DMASnBr_3$ at HSE06-SOC level of theory; PBE/HSE06-SOC band edges; supercells employed to simulate slabs of models A(A′)/B(B′); structures and charge localization for defective slabs; additional references (PDF)

AUTHOR INFORMATION

Corresponding Authors

Francesco Ambrosio − *Computational Laboratory for Hybrid/Organic Photovoltaics (CLHYO), Istituto CNR di Scienze e Tecnologie Chimiche "Giulio Natta" (CNR-SCITEC), 06123 Perugia, Italy; Department of Chemistry and Biology "A. Zambelli", University of Salerno, 84084 Fisciano, Salerno, Italy; CNST@PoliMi, Istituto Italiano di Tecnologia, 20133 Milano, Italy;* orcid.org/0000-0002-6388-9586; Email: fambrosio@unisa.it

Filippo De Angelis − *Department of Chemistry, Biology and Biotechnology, University of Perugia, 06123 Perugia, Italy; Computational Laboratory for Hybrid/Organic Photovoltaics (CLHYO), Istituto CNR di Scienze e Tecnologie Chimiche "Giulio Natta" (CNR-SCITEC), 06123 Perugia, Italy; Department of Natural Sciences & Mathematics, College of Sciences & Human Studies, Prince Mohammad Bin Fahd University, Al Khobar 31952, Saudi Arabia;* orcid.org/0000-0003-3833-1975; Email: filippo@thch.unipg.it

Authors

Damiano Ricciarelli − *Department of Chemistry, Biology and Biotechnology, University of Perugia, 06123 Perugia, Italy; Computational Laboratory for Hybrid/Organic Photovoltaics (CLHYO), Istituto CNR di Scienze e Tecnologie Chimiche "Giulio Natta" (CNR-SCITEC), 06123 Perugia, Italy;* orcid.org/0000-0003-4213-2514

Waldemar Kaiser − *Computational Laboratory for Hybrid/Organic Photovoltaics (CLHYO), Istituto CNR di Scienze e Tecnologie Chimiche "Giulio Natta" (CNR-SCITEC), 06123 Perugia, Italy*

Edoardo Mosconi − *Computational Laboratory for Hybrid/Organic Photovoltaics (CLHYO), Istituto CNR di Scienze e Tecnologie Chimiche "Giulio Natta" (CNR-SCITEC), 06123 Perugia, Italy;* orcid.org/0000-0001-5075-6664

Julia Wiktor − *Department of Physics, Chalmers University of Technology, 412 96 Goteborg, Sweden;* orcid.org/0000-0003-3395-1104

Muhammad Waqar Ashraf − *Department of Natural Sciences & Mathematics, College of Sciences & Human Studies, Prince Mohammad Bin Fahd University, Al Khobar 31952, Saudi Arabia*

Lorenzo Malavasi − *Department of Chemistry and INSTM, Università degli Studi di Pavia, Pavia 27100, Italy;* orcid.org/0000-0003-4724-2376

Complete contact information is available at: https://pubs.acs.org/10.1021/acsenergylett.2c00122

Notes

The authors declare no competing financial interest.

ACKNOWLEDGMENTS

The Ministero dell'Istruzione dell'Università e della Ricerca (MIUR) and Università degli Studi di Perugia are acknowledged for financial support through the program "Dipartimenti di Eccellenza 2018−2022" (Grant AMIS). This research was funded by PON Project "Tecnologia per celle solari bifacciali ad alta Efficienza a 4 terminali per utility scale" (BEST-4U), of the Italian Ministry MIUR (CUP B88D19000160005) and by project Ricerca@Cnr PHOTOCAT (CUP B93C210000060006). JW acknowledges funding from the Swedish Research Council (2019-03993) and the Chalmers Gender Initiative for Excellence (Genie). FA acknowledges support from by the European Union's Horizon 2020 research and innovation programme under grant agreement No 771528 of the SOPHY project.

REFERENCES

(1) Edri, E. E.; Kirmayer, S.; Mukhopadhyay, K.; Gartsman, G.; Hodes; Cahen, D. Elucidating the charge carrier separation and working mechanism of $CH_3NH_3PbI_3$− xCl_x perovskite solar cells. *Nat. Commun.* **2014**, *5*, 3461.

(2) Hutter, E. M.; Gélvez-Rueda, M. C.; Osherov, A.; Bulović, V.; Grozema, F. C.; Stranks, S. D.; Savenije, T. J. Direct−indirect character of the bandgap in methylammonium lead iodide perovskite. *Nat. Mater.* **2017**, *16*, 115.

(3) Crothers, T. W.; Milot, R. L.; Patel, J. B.; Parrott, E. S.; Schlipf, J.; Müller-Buschbaum, P.; Johnston, M. B.; Herz, L. M. Photon Reabsorption Masks Intrinsic Bimolecular Charge-Carrier Recombination in $CH_3NH_3PbI_3$ Perovskite. *Nano Lett.* **2017**, *17*, 5782−5789.

(4) Ambrosio, F.; Wiktor, J.; De Angelis, F.; Pasquarello, A. Origin of low electron−hole recombination rate in metal halide perovskites. *Energy Environ. Sci.* **2018**, *11*, 101−105.

(5) Ambrosio, F.; Meggiolaro, D.; Mosconi, E.; De Angelis, F. Charge Localization, Stabilization, and Hopping in Lead Halide Perovskites: Competition between Polaron Stabilization and Cation Disorder. *ACS Energy Lett.* **2019**, *4*, 2013−2020.

(6) Motti, S. G.; Meggiolaro, D.; Martani, S.; Sorrentino, R.; Barker, A. J.; De Angelis, F.; Petrozza, A. Defect Activity in Metal−Halide Perovskites. *Adv. Mater.* **2019**, *31*, 1901183.

(7) Kim, J.; Lee, S.-H.; Lee, J. H.; Hong, K.-H. The Role of Intrinsic Defects in Methylammonium Lead Iodide Perovskite. *J. Phys. Chem. Lett.* **2014**, *5*, 1312−1317.

(8) Dagnall, K. A.; Foley, B. J.; Cuthriell, S. A.; Alpert, M. R.; Deng, X.; Chen, A. Z.; Sun, Z.; Gupta, M. C.; Xiao, K.; Lee, S.-H.; et al. Relationship between the Nature of Monovalent Cations and Charge Recombination in Metal Halide Perovskites. *ACS Appl. Energy Mater.* **2020**, *3*, 1298−1304.

(9) Chu, W.; Zheng, Q.; Prezhdo, O. V.; Zhao, J.; Saidi, W. A. Low-frequency lattice phonons in halide perovskites explain high defect tolerance toward electron-hole recombination. *Sci. Adv.* **2020**, *6*, eaaw7453.

(10) Chu, W.; Saidi, W. A.; Zhao, J.; Prezhdo, O. V. Soft Lattice and Defect Covalency Rationalize Tolerance of *β*-CsPbI3 Perovskite Solar Cells to Native Defects. *Angew. Chem., Int. Ed.* **2020**, *59*, 6435−6441.

(11) Brenner, T. M.; Egger, D. A.; Kronik, L.; Hodes, G.; Cahen, D. Hybrid organic−inorganic perovskites: low-cost semiconductors with intriguing charge-transport properties. *Nat. Rev. Mater.* **2016**, *1*, 15007.

(12) Meggiolaro, D.; Ambrosio, F.; Mosconi, E.; Mahata, A.; De Angelis, F. Polarons in Metal Halide Perovskites. *Adv. Energy Mater.* **2020**, *10*, 1902748.

(13) Ponseca, C. S.; Savenije, T. J.; Abdellah, M.; Zheng, K.; Yartsev, A.; Pascher, T.; Harlang, T.; Chabera, P.; Pullerits, T.; Stepanov, A.; et al. Organometal Halide Perovskite Solar Cell Materials Rationalized: Ultrafast Charge Generation, High and Microsecond-Long Balanced Mobilities, and Slow Recombination. *J. Am. Chem. Soc.* **2014**, *136*, 5189−5192.

(14) Yamada, Y.; Endo, M.; Wakamiya, A.; Kanemitsu, Y. Spontaneous Defect Annihilation in $CH_3NH_3PbI_3$ Thin Films at Room Temperature Revealed by Time-Resolved Photoluminescence Spectroscopy. *J. Phys. Chem. Lett.* **2015**, *6*, 482−486.

(15) Buin, A.; Pietsch, P.; Xu, J.; Voznyy, O.; Ip, A. H.; Comin, R.; Sargent, E. H. Materials Processing Routes to Trap-Free Halide Perovskites. *Nano Lett.* **2014**, *14*, 6281−6286.
(16) Meggiolaro, D.; Motti, S. G.; Mosconi, E.; Barker, A. J.; Ball, J.; Andrea Riccardo Perini, C.; Deschler, F.; Petrozza, A.; De Angelis, F. Iodine chemistry determines the defect tolerance of lead-halide perovskites. *Energy Environ. Sci.* **2018**, *11*, 702−713.
(17) Kojima, A.; Teshima, K.; Shirai, Y.; Miyasaka, T. Organometal Halide Perovskites as Visible-Light Sensitizers for Photovoltaic Cells. *J. Am. Chem. Soc.* **2009**, *131*, 6050−6051.
(18) Kim, H.-S.; Lee, C.-R.; Im, J.-H.; Lee, K.-B.; Moehl, T.; Marchioro, A.; Moon, S.-J.; Humphry-Baker, R.; Yum, J.-H.; Moser, J. E.; Gratzel, M.; Park, N.-G.; et al. Lead Iodide Perovskite Sensitized All-Solid-State Submicron Thin Film Mesoscopic Solar Cell with Efficiency Exceeding 9%. *Sci. Rep.* **2012**, *2*, 591.
(19) Etgar, L.; Gao, P.; Xue, Z.; Peng, Q.; Chandiran, A. K.; Liu, B.; Nazeeruddin, M. K.; Grätzel, M. Mesoscopic $CH_3NH_3PbI_3/TiO_2$ Heterojunction Solar Cells. *J. Am. Chem. Soc.* **2012**, *134*, 17396−17399.
(20) Burschka, J.; Pellet, N.; Moon, S.-J.; Humphry-Baker, R.; Gao, P.; Nazeeruddin, M. K.; Gratzel, M. Sequential deposition as a route to high-performance perovskite-sensitized solar cells. *Nature* **2013**, *499*, 316−319.
(21) Stranks, S. D.; Eperon, G. E.; Grancini, G.; Menelaou, C.; Alcocer, M. J. P.; Leijtens, T.; Herz, L. M.; Petrozza, A.; Snaith, H. J. Electron-Hole Diffusion Lengths Exceeding 1 Micrometer in an Organometal Trihalide Perovskite Absorber. *Science* **2013**, *342*, 341−344.
(22) *Best Researvh-Cell Efficiencies*, National Renewable Energy Laboratory (NREL); https://www.nrel.gov/pv/assets/images/efficiency-chart.png (access date 2021-12-10).
(23) Yoo, J. J.; Seo, G.; Chua, M. R.; Park, T. G.; Lu, Y.; Rotermund, F.; Kim, Y.-K.; Moon, C. S.; Jeon, N. J.; Correa-Baena, J.-P.; et al. Efficient perovskite solar cells via improved carrier management. *Nature* **2021**, *590*, 587−593.
(24) Noel, N. K.; Stranks, S. D.; Abate, A.; Wehrenfennig, C.; Guarnera, S.; Haghighirad, A.-A.; Sadhanala, A.; Eperon, G. E.; Pathak, S. K.; Johnston, M. B.; et al. Lead-free organic-inorganic tin halide perovskites for photovoltaic applications. *Energy Environ. Sci.* **2014**, *7*, 3061−3068.
(25) Hao, F.; Stoumpos, C. C.; Cao, D. H.; Chang, R. P. H.; Kanatzidis, M. G. Lead-free solid-state organic−inorganic halide perovskite solar cells. *Nat. Photonics* **2014**, *8*, 489−494.
(26) Umari, P.; Mosconi, E.; De Angelis, F. Relativistic GW calculations on $CH_3NH_3PbI_3$ and $CH_3NH_3SnI_3$ Perovskites for Solar Cell Applications. *Sci. Rep.* **2015**, *4*, 4467.
(27) Mosconi, E.; Umari, P.; De Angelis, F. Electronic and optical properties of mixed Sn-Pb organohalide perovskites: a first principles investigation. *J. Mater. Chem. A* **2015**, *3*, 9208−9215.
(28) Ricciarelli, D.; Meggiolaro, D.; Ambrosio, F.; De Angelis, F. Instability of Tin Iodide Perovskites: Bulk p-Doping versus Surface Tin Oxidation. *ACS Energy Lett.* **2020**, *5*, 2787−2795.
(29) Meggiolaro, D.; Ricciarelli, D.; Alasmari, A. A.; Alasmary, F. A. S.; De Angelis, F. Tin versus Lead Redox Chemistry Modulates Charge Trapping and Self-Doping in Tin/Lead Iodide Perovskites. *J. Phys. Chem. Lett.* **2020**, *11*, 3546−3556.
(30) Dalpian, G. M.; Liu, Q.; Stoumpos, C. C.; Douvalis, A. P.; Balasubramanian, M.; Kanatzidis, M. G.; Zunger, A. Changes in charge density vs changes in formal oxidation states: The case of Sn halide perovskites and their ordered vacancy analogues. *Phys. Rev. Mater.* **2017**, *1*, 025401.
(31) Bowman, A. R.; Klug, M. T.; Doherty, T. A. S.; Farrar, M. D.; Senanayak, S. P.; Wenger, B.; Divitini, G.; Booker, E. P.; Andaji-Garmaroudi, Z.; Macpherson, S.; et al. Microsecond Carrier Lifetimes, Controlled p-Doping, and Enhanced Air Stability in Low-Bandgap Metal Halide Perovskites. *ACS Energy Lett.* **2019**, *4*, 2301−2307.
(32) Filip, M. R.; Eperon, G. E.; Snaith, H. J.; Giustino, F. Steric engineering of metal-halide perovskites with tunable optical band gaps. *Nat. Commun.* **2014**, *5*, 5757.
(33) Ouhbi, H.; Ambrosio, F.; De Angelis, F.; Wiktor, J. Strong Electron Localization in Tin Halide Perovskites. *J. Phys. Chem. Lett.* **2021**, *12*, 5339−5343.
(34) Naveen Kumar, T. R.; Karthik, P.; Neppolian, B. Polaron and bipolaron induced charge carrier transportation for enhanced photocatalytic H_2 production. *Nanoscale* **2020**, *12*, 14213−14221.
(35) Zhang, L.; Chu, W.; Zhao, C.; Zheng, Q.; Prezhdo, O. V.; Zhao, J. Dynamics of Photoexcited Small Polarons in Transition-Metal Oxides. *J. Phys. Chem. Lett.* **2021**, *12*, 2191−2198.
(36) Pastor, E.; Park, J.-S.; Steier, L.; Kim, S.; Grätzel, M.; Durrant, J. R.; Walsh, A.; Bakulin, A. A. In situ observation of picosecond polaron self-localisation in α-Fe_2O_3 photoelectrochemical cells. *Nat. Commun.* **2019**, *10*, 3962.
(37) Ambrosio, F.; Wiktor, J. Strong Hole Trapping Due to Oxygen Dimers in $BiVO_4$: Effect on the Water Oxidation Reaction. *J. Phys. Chem. lett.* **2019**, *10*, 7113−7118.
(38) Wiktor, J.; Ambrosio, F.; Pasquarello, A. Role of Polarons in Water Splitting: The Case of $BiVO_4$. *ACS Energy Lett.* **2018**, *3*, 1693−1697.
(39) Gono, P.; Wiktor, J.; Ambrosio, F.; Pasquarello, A. Surface Polarons Reducing Overpotentials in the Oxygen Evolution Reaction. *ACS Catal.* **2018**, *8*, 5847−5851.
(40) Huang, H.; Pradhan, B.; Hofkens, J.; Roeffaers, M. B. J.; Steele, J. A. Solar-Driven Metal Halide Perovskite Photocatalysis: Design, Stability, and Performance. *ACS Energy Lett.* **2020**, *5*, 1107−1123.
(41) Bisquert, J.; Juarez-Perez, E. J. The Causes of Degradation of Perovskite Solar Cells. *J. Phys. Chem. Lett.* **2019**, *10*, 5889−5891.
(42) Khlyabich, P. P.; Hamill, J. C.; Loo, Y.-L. Precursor Solution Annealing Forms Cubic-Phase Perovskite and Improves Humidity Resistance of Solar Cells. *Adv. Funct. Mater.* **2018**, *28*, 1801508.
(43) Zheng, C.; Rubel, O. Unraveling the Water Degradation Mechanism of $CH_3NH_3PbI_3$. *J. Phys. Chem. Lett.* **2019**, *123*, 19385−19394.
(44) Leguy, A.; Hu, Y.; Campoy-Quiles, M.; Alonso, M. I.; Weber, O. J.; Azarhoosh, P.; van Schilfgaarde, M.; Weller, M. T.; Bein, T.; Nelson, J.; et al. The Reversible Hydration of $CH_3NH_3PbI_3$ in Films, Single Crystals and Solar Cells. *Chem. Mater.* **2015**, *27*, 3397−3407.
(45) Mosconi, E.; Azpiroz, J. M.; De Angelis, F. Ab Initio Molecular Dynamics Simulations of Methylammonium Lead Iodide Perovskite Degradation by Water. *Chem. Mater.* **2015**, *27*, 4885−4892.
(46) Romani, L.; Speltini, A.; Ambrosio, F.; Mosconi, E.; Profumo, A.; Marelli, M.; Margadonna, S.; Milella, A.; Fracassi, F.; Listorti, A.; et al. Water-Stable $DMASnBr_3$ Lead-Free Perovskite for Effective Solar-Driven Photocatalysis. *Angew. Chem., Int. Ed.* **2021**, *60*, 3611−3618.
(47) Pisanu, A.; Speltini, A.; Quadrelli, P.; Drera, G.; Sangaletti, L.; Malavasi, L. Enhanced air-stability of Sn-based hybrid perovskites induced by dimethylammonium (DMA): synthesis, characterization, aging and hydrogen photogeneration of the $MA_{1-x}DMA_xSnBr_3$ system. *J. Mater. Chem. C* **2019**, *7*, 7020−7026.
(48) Chen, G.; Wang, P.; Wu, Y.; Zhang, Q.; Wu, Q.; Wang, Z.; Zheng, Z.; Liu, Y.; Dai, Y.; Huang, B. Lead-Free Halide Perovskite $Cs_3Bi_{2x}Sb_{2-2x}I_9$ ($x \approx 0.3$) Possessing the Photocatalytic Activity for Hydrogen Evolution Comparable to that of $(CH_3NH_3)PbI_3$. *Adv. Mater.* **2020**, *32*, 2001344.
(49) Zhao, H.; Li, Y.; Zhang, B.; Xu, T.; Wang, C. $PtI_x/[(CH_3)_2NH_2]_3[BiI_6]$ as a well-dispersed photocatalyst for hydrogen production in hydroiodic acid. *Nano Energy* **2018**, *50*, 665−674.
(50) Romani, L.; Bala, A.; Kumar, V.; Speltini, A.; Milella, A.; Fracassi, F.; Listorti, A.; Profumo, A.; Malavasi, L. PEA_2SnBr_4: a water-stable lead-free two-dimensional perovskite and demonstration of its use as a co-catalyst in hydrogen photogeneration and organic-dye degradation. *J. Mater. Chem. C* **2020**, *8*, 9189−9194.
(51) Armenise, V.; Colella, S.; Fracassi, F.; Listorti, A. Lead-Free Metal Halide Perovskites for Hydrogen Evolution from Aqueous Solutions. *Nanomater.* **2021**, *11*, 433.
(52) Ju, D.; Zheng, X.; Liu, J.; Chen, Y.; Zhang, J.; Cao, B.; Xiao, H.; Mohammed, O. F.; Bakr, O. M.; Tao, X. Reversible Band Gap Narrowing of Sn-Based Hybrid Perovskite Single Crystal with

https://doi.org/10.1021/acsenergylett.2c00122
ACS Energy Lett. 2022, 7, 1308−1315

Excellent Phase Stability. *Angew. Chem., Int. Ed.* **2018**, *57*, 14868−14872.
(53) Daub, M.; Hillebrecht, H. On the Demystification of "$HPbI_3$" and the Peculiarities of the Non-innocent Solvents H_2O and DMF. *Z. Anorg. Allg. Chem.* **2018**, *644*, 1393−1400.
(54) Heyd, J.; Scuseria, G. E.; Ernzerhof, M. Hybrid functionals based on a screened Coulomb potential. *J. Chem. Phys.* **2003**, *118*, 8207−8215.
(55) Corso, A. D.; Conte, A. M. Spin-orbit coupling with ultrasoft pseudopotentials: Application to Au and Pt. *Phys. Rev. B* **2005**, *71*, 115106.
(56) Coduri, M.; Strobel, T. A.; Szafrański, M.; Katrusiak, A.; Mahata, A.; Cova, F.; Bonomi, S.; Mosconi, E.; De Angelis, F.; Malavasi, L. Band Gap Engineering in MASnBr3 and CsSnBr3 Perovskites: Mechanistic Insights through the Application of Pressure. *J. Phys. Chem. Lett.* **2019**, *10*, 7398−7405.
(57) Perdew, J. P.; Burke, K.; Ernzerhof, M. Generalized Gradient Approximation Made Simple. *Phys. Rev. Lett.* **1996**, *77*, 3865−3868.
(58) Walsh, A.; Scanlon, D. O.; Chen, S.; Gong, X. G.; Wei, S.-H. Self-Regulation Mechanism for Charged Point Defects in Hybrid Halide Perovskites. *Angew. Chem., Int. Ed.* **2015**, *54*, 1791−1794.
(59) Freysoldt, C.; Neugebauer, J. First-principles calculations for charged defects at surfaces, interfaces, and two-dimensional materials in the presence of electric fields. *Phys. Rev. B* **2018**, *97*, 205425.

https://doi.org/10.1021/acsenergylett.2c00122
ACS Energy Lett. 2022, 7, 1308−1315